International Journal of Refrigeration 106 (2019) 526–538

Contents lists available at ScienceDirect

International Journal of Refrigeration

journal homepage: www.elsevier.com/locate/ijrefrig

An open-source density-based solver for two-phase CO_2 compressible flows: Verification and validation

Yu Fang[a,b,*], Sébastien Poncet[a], Hakim Nesreddine[c], Yann Bartosiewicz[b]

[a] Département de génie mécanique, Université de Sherbrooke, 2500 boulevard de l'Université, Sherbrooke. (QC) J1K 2R1, Canada
[b] Institute Mechanics, Materials, and Civil Engineering (iMMC), Université catholique de Louvain (UCLouvain), Louvain-la-Neuve 1348, Belgium
[c] Laboratoire des technologies de l'énergie, Shawinigan, Québec, Canada

ARTICLE INFO

Article history:
Available online 18 May 2019

Keywords:
Two-phase CO_2 flow
Flashing nozzle
Real gas properties
Compressible solver
Tabulated method

ABSTRACT

A density-based solver based on the OpenFoam library coupled with a tabulated equation of state is developed. The Navier–Stokes characteristic boundary condition is considered to guarantee the accuracy and stability of the simulation. Firstly, two validation test cases are considered to illustrate the solver capability. Then, the flows in two converging-diverging nozzles are simulated under supercritical and subcritical conditions. A good agreement in terms of pressure distribution is obtained for all nozzles. The bulk viscosity and turbulence effects are then carefully assessed. The bulk viscosity does not affect significantly the predictions of the new solver, whereas it is of prime importance to well model the thermal and flow fields up to the wall. Finally, it is recommended to use an unsteady density-based solver for CO_2 flows in converging-diverging nozzles associated with a Homogeneous Equilibrium Model and the k-ω SST closure to get the best overall predictions.

Solveur open-source basé sur la densité pour les flux compressibles diphasiques de CO_2: Vérification et validation

Mots-clés: Écoulement diphasique de CO_2; Tuyère avec vaporisation instantanée; Propriétés des gaz réels; Solveur compressible; Méthode compilée

1. Introduction

According to the present European legislation (Regulations EC No 2037/2000 and No 842/2006) (European Parliament and the Council, 2014; The National Archives, 2006), the refrigerants bearing a high Global Warning Potential (GWP higher than 150), and high ozone depletion potential (ODP) will be phased out later in 2025. It means that most of current synthetic refrigerants which are commonly used for the refrigeration, air-conditioning, and heat pump industries, will be banned. Carbon dioxide (denoted as CO_2) as a natural fluid possesses zero ODP and low GWP as well as non-toxic and non-flammable characteristics, and is thus considered as a potential alternative to CFCs and HCFCs refrigerants in the future. Masson et al. (2014) indicated that CO_2 is increasingly applied for refrigeration applications in European supermarkets (increase of 117% between 2011 and 2013). However, the main issue of applying CO_2 in a vapor-compression cycle is that the system efficiency (or its coefficient of performance, COP) is relatively low, especially when operating in transcritical conditions. A promising way to improve its COP is to replace the conventional expansion valve by an ejector. It can reduce significantly both the throttling losses and the compressor load (Lorentzen, 1983). The ejector-expansion CO_2 transcritical refrigeration cycle (EERC) was firstly proposed by Liu et al. (2002) and then extensively investigated during the past few years. The experimental investigations on the CO_2 transcritical cycle by Elbel and Hrnjak (2008) reported an improvement in terms of COP and cooling capacity by 7% and 8%, respectively. Furthermore, Li and Groll (2004) confirmed a COP improvement up to 16% based on a constant pressure mixing model. Besides, Deng et al. (2007) analyzed the CO_2 transcritical EERC by means of a

* Corresponding author at: Département de génie mécanique, Université de Sherbrooke, 2500 boulevard de l'Université, Sherbrooke. (QC) J1K 2R1, Canada.
E-mail addresses: yu.fang@usherbrooke.ca, yu.fang@uclouvain.be (Y. Fang).

https://doi.org/10.1016/j.ijrefrig.2019.05.016
0140-7007/

thermodynamic model and an improvement of 22% and 11.5% in terms of COP and cooling capacity were obtained respectively. CO_2 multi-ejector systems have also been proposed for the supermarket applications (Hafner et al., 2014). Through transient simulations, COP improvement up to 30% was obtained (Hafner et al., 2014). An R744 vapour compression rack equipped with multi-ejector expansion pack was investigated experimentally by Haida et al. (2016). Again, an improvement of COP up to 7% was obtained for transcritical conditions.

The previous studies are mainly concerned with global performance parameters, such as the COP, cooling capacity, entrainment ratio, and pressure ratio. Recently, more attention has been paid to the detailed flow fields within CO_2 two-phase ejectors by means of Computational Fluid Dynamics (CFD) simulations. CFD allows to provide a fundamental understanding of the complex phenomena within the ejector. Smolka et al. (2013) proposed an enthalpy-based energy equation to replace the temperature-based energy equation within ANSYS Fluent (ANSYS, 2010). The homogeneous equilibrium model (HEM) was coupled with the Refprop database (Lemmon et al., 2010) for the property calculation and with a pressure-based solver. Pressure is then coupled with the velocity field, whereas density is computed by the EoS. The mass flowrate agreed well with the experimental measurements, whereas a large discrepancy was obtained for the pressure distribution within the mixing chamber of the transcritical CO_2 ejector. A similar approach has been used by Palacz et al. (2015) to analyze the accuracy of the HEM for two-phase CO_2 ejectors for supermarket refrigeration applications. A better agreement in terms of mass flowrate was obtained for operating conditions close or above the critical point. Lucas et al. (2014) also developed a pressure-based solver coupled with the HEM using the OpenFOAM library. The authors obtained a 10% (resp. 20%) error in terms of pressure recovery without (resp. with) suction flow for a two-phase CO_2 ejector. The Homogeneous Relaxation Model (HRM) was also applied for CO_2 two-phase ejectors by Colarossi et al. (2012). They reported an average error of 18.6% in terms of pressure differences between the inlets and outlet. They attributed these discrepancies to first the choice of the k-ε turbulence model and then to the imposed boundary conditions, namely a fixed mass flowrate with a zero gradient pressure boundary condition at the inlets and a zero velocity gradient with a non-reflecting pressure boundary condition at the outlet. Palacz et al. (2016) compared the predictions of the HEM and HRM for two-phase CO_2 ejectors for supermarket refrigeration applications. Their numerical results were compared to experimental ones in terms of entrainment ratio and primary mass flowrate. For operating conditions above the critical point, the HEM is found to be more accurate than the HRM, while for operating conditions far below the critical point, the HRM performed around 5% better than the HEM in terms of primary mass flow rate. Haida et al. (2018) proposed a modified HRM in which the relaxation time was optimised through a genetic algorithm. A short relaxation time was obtained for the supercritical and transcritical regimes, such that the modified HRM tends to the HEM. A higher relaxation time was obtained for pressures lower than 5.9 MPa leading to relative errors in terms of primary mass flowrate below 15%.

The heat and mass transfer mechanisms within a two-phase CO_2 ejector are extremely complex to capture and understand: transient phase change (flashing), turbulent mixing, condensation, evaporation, two phase interactions, shock waves and shock-boundary layer interactions. In terms of numerical method, each mechanism mentioned above can affect significantly the predictions of the CFD tools. The inaccurate prediction of one mechanism can lead to poor predictions, whereas the inaccurate predictions of two different mechanisms can compensate each other and lead to satisfactory results in terms of global parameters. Most of the open literature on two-phase CO_2 ejectors for refrigeration applications has been published based on pressure-based solvers, whereas it is now well known in the fluid mechanics community that density-based flow solvers are required for high compressible flows. They have been indeed extensively used for water transient simulations, combustion applications, and single-phase ejectors. On the contrary, no CFD simulations based on a density-based solver have been performed for transcritical CO_2 ejectors, which is mainly due to numerical stability issues of commercial solvers and their uncapacity to couple a density-based solver with external real gas properties such as the Refprop or any other external subroutines. The prediction of compressible flows is based on a good resolution and capture of acoustic waves and their speeds of propagation within the flow. Though the pressure-based solver with some compressible corrections could perform relatively well for weakly compressible flows, it cannot accurately predict the flow field for highly compressible flows, such as for transcritical CO_2 ejectors. Hence, in the present work, the authors develop a new density-based flow solver based on *rhoCentralFoam* proposed in the OpenFOAM library. The present solver is based on a conservative formulation, which guarantees to correctly capture the acoustic waves within the computational domain. The thermodynamic properties are computed by an accurate and efficient look-up table equation of state (EoS) based on Span-Wagner EoS (Span and Wagner, 1994) and covering the supercritical, vapor, liquid and vapor-liquid states of CO_2. Another important issue for a compressible solver is the treatment of boundary conditions. Inappropriate inlet and outlet boundary conditions can indeed generate non-physical waves in the computational domain. Depending on the numerical scheme, if these numerical waves are not dissipated, they accumulate and may lead to the divergence of the simulation. Hence, the Navier–Stokes characteristic boundary condition (NSCBC) is firstly implemented for the outlet boundary, which insures the correct ingoing and outgoing of acoustic waves at the boundary and so enhances the stability of the simulation. It should be noted that the NSCBC is also coupled with EoS in order to compute the ingoing and outgoing waves.

Converging-diverging Laval nozzles are simulated and presented in the following sections, as it constitutes a first and necessary step towards the modeling of a full supersonic ejector. It transforms the pressure energy of the primary flow into kinetic energy. As a result, the flow becomes supersonic. Meanwhile, due to the pressure drop, the flashing occurs near the throat. Eventually, a low-pressure supersonic two-phase jet at outlet of the primary nozzle is obtained which entrains the high-pressure secondary flow. Hence, the flow condition at the outlet of the primary nozzle affects considerably the entrainment of the secondary flow and the mixing phenomenon in the mixing chamber and diffuser. The CO_2 converging-diverging nozzle has been extensively investigated experimentally and numerically. Nakagawa et al. (2009b) provided a very useful experimental database in terms of pressure and temperature distributions for benchmarking purpose. According to their measurements, the flow in the diverging part was nearly in thermodynamic equilibrium for supercritical ($p = 9.1$ MPa), transcritical ($p = 7.1$ MPa) and subcritical ($p = 6.1$ MPa) conditions and diverging angles ranging from 0.076^o to 0.612^o. Berana et al. (2009) measured the pressure distributions along the nozzle with and without the appearance of shock waves. The pseudo-shock and dispersed shock waves were obtained, which are much thicker and weaker than equilibrium shock waves (Berana et al., 2009). The two-phase CO_2 nozzle was investigated by flow visualizations by Li et al. (2018). They revealed that the phase-change position can be after or before the nozzle throat depending on the operating conditions. Angielczyk et al. (2010) proposed a 1D HRM model for CO_2 nozzle simulations. A good agreement was obtained in (Angielczyk et al., 2010) for nozzles with large diverging angles compared to Nakagawa et al. (2009a) 's measurements. However, large discrep-

ancies were obtained for the nozzles with small diverging angles. Yazdani et al. (2014) considered the cavitation and boiling phase-change phenomena in their simulations. The pressure-based solver in ANSYS Fluent was used to simulate one small and one large diverging angle nozzle. A good agreement in terms of pressure distribution was obtained compared to the experimental measurements of Nakagawa et al. (2009a). However, some shock waves were observed at the outlet, which could be related to the inappropriate choice of boundary condition. Ameli et al. (2017) simulated the nozzle of Berana et al. (2009) using ANSYS CFX. The Refprop database was used to build a Real Gas Properties (RGP) table embedded within ANSYS CFX. Though the pressure distribution was well predicted, an abnormal shock wave was predicted near the outlet, which may be attributed to unappropriate outlet boundary condition. Raman and Kim (2018) used a 1D gas dynamic model to simulate the shock waves within the nozzle. Different EoS were assessed and showed a significant influence on the prediction of the shock wave position. However, their operating conditions were based on the pressure ratio rather than the real pressures imposed in Berana et al. (2009). The small angle nozzles in Nakagawa et al. (2009a) were investigated by Giacomelli et al. (2018). A tabulated property calculation approach based on Refprop was coupled with the pressure-based solver of ANSYS Fluent. The sensitivity to different types of boundary condition was analyzed without exhibiting significant difference. However, an unphysical pressure drop was predicted at the outlet in all cases. The accommodation coefficient for the evaporation was calibrated based on subcritical conditions (Giacomelli et al., 2018). Better results were obtained for larger diverging angles. The Wallis' formulation available within ANSYS Fluent (ANSYS, 2010) and Yazdani's formulation (Yazdani et al., 2014) for the Mach number were also compared revealing a significant difference (Giacomelli et al., 2018). The default formulation predicts a subsonic nozzle with a normal shock at the outlet, while Yazdani's formulation predicts the supersonic flow after the throat (Giacomelli et al., 2018). As the authors mentioned in (Giacomelli et al., 2018), the speed of sound is not involved in the simulation, except for the pressure-correction equation. Generally, the pressure-based solver does not deal with the acoustic waves travelling within the computational domain, therefore the sound speed is not required. However, the pressure-correction equation is crucial when dealing with compressible flows. As the information is not currently available within ANSYS Fluent, the evaluation of the default sound speed formulation is difficult. On the contrary, for density-based solvers, the sound speed is required by the solver to estimate numerically the wave propagation speed and is most of the time computed by the EoS. The wave propagation speed is besides intrinsic for hyperbolic systems, therefore the choice of the sound speed formulation should not affect the final converged solution.

The objective of the present work is to propose a new flow solver developed under the OpenFOAM library. All the different ingredients (two-phase model, fluid properties, bulk viscosity, turbulence model, 2D/3D, boundary conditions) are introduced in detail, carefully validated and discussed to clearly demonstrate the appropriate way to build a new solver for such complex flows. To the best of the authors' knowledge, such a detailed numerical analysis has never been published to date.

The organisation of this paper is as follows: In Section 2, the numerical method is first described. It consists of the two-phase model, the density-based solver, the real gas approach, and the NSCBC boundary condition. Then, in Section 3, two classical test cases are considered to validate the density-based solver, namely the shock tube and the depressurization. In Section 4, two different converging-diverging Laval nozzles are simulated under supercritical and subcritical operating conditions. The pressure profiles are compared against the numerical and experimental results of Nakagawa et al. (2009a). Then, the bulk viscosity and turbulence effects are analyzed in detail.

2. Numerical modeling

2.1. Homogeneous Equilibrium Model (HEM)

Numerous two-phase models have been proposed in the literature, from the most complete one which assumes two separate phases (Pelanti and Shyue, 2014; Saurel et al., 2009) being fully in thermodynamic and mechanical non-equilibrium (Bilicki and Kestin, 1990) to the simplest one which considers only the mixture with fully equilibrium between the two phases (Baer and Nunziato, 1986). In the context of two-phase CO_2 supersonic ejectors, the most considered two-phase model is the HEM (Lucas et al., 2014; Palacz et al., 2015; Smolka et al., 2013). Palacz et al. (2016) obtained good results with the HEM in supercritical and transcritical operating conditions. In the optimised HRM proposed by Haida et al. (2018), the HEM provide the results as good as the HRM in relevant operating conditions. Angielczyk et al. (2010) also obtained similar results between the HEM and HRM for simulations of Nakagawa nozzle (Nakagawa et al., 2009a). Hence, for sake of the simplicity, in the present study the HEM is considered to predict the flashing phenomenon in the ejector's primary nozzle, which determines the two-phase flow condition at its outlet.

As mentioned above, the HEM assumes the fully thermodynamic and mechanical equilibrium between the gas and liquid phases, which means that the two phases share the same temperature, pressure and velocity. Hence, it can be defined by a set of three partial differential equations consisting of the conservation of mass (Eq. (1)), the conservation of momentum (Eq. (2)) and the conservation of total energy (Eq. (3)) for the two-phase mixture. The set of equations writes

$$\frac{\partial \rho}{\partial t} + \nabla \cdot (\rho \mathbf{u}) = 0, \tag{1}$$

$$\frac{\partial \rho \mathbf{u}}{\partial t} + \nabla \cdot (\rho \mathbf{u}\mathbf{u} + p\mathbf{I}) = 0, \tag{2}$$

$$\frac{\partial \rho E}{\partial t} + \nabla \cdot [(\rho E + p)\mathbf{u})] = 0. \tag{3}$$

The system is written under its conservation form and the conservative variables are: ρ the density, $\rho\mathbf{u}$ the momentum and ρE the total energy of the mixture. u and E denote the velocity of the mixture and its specific total energy, respectively, $E = e + |\mathbf{u}|^2/2$, where e is the specific internal energy. This non-linear hyperbolic conservative equation system governs the dynamics of the inviscid, and adiabatic compressible two-phase flow without body forces. It has formally the same structure as the single-phase Euler system. It can be solved by *rhoCentralFoam* solver in the OpenFOAM library. Additionally, the viscous effect can also be considered by the solver, such that the flow is governed by the Navier–Stokes equations. The treatment of the viscous dissipation terms are discussed in Section 2.2.

The fully thermodynamic and mechanical equilibrium assumed in HEM leads to the following constraints:

$$\begin{aligned} p_l &= p_v = p_{sat}, \\ T_l &= T_v = T_{sat}, \\ u_l &= u_v = u, \\ g_l &= g_v = g, \end{aligned} \tag{4}$$

where the subscripts l and v denote the liquid and the vapor phases, respectively. The term g represents the specific Gibbs free energy, $g = h - Ts$, where h is the specific enthalpy, T is the temperature and s is the specific entropy. For two-phase states, the liquid and the vapor are saturated, with the specific internal energy

and the specific volume of the mixture being:

$$e = x\,e_v + (1-x)\,e_l,$$
$$v = x\,v_v + (1-x)\,v_l, \tag{5}$$

where e_l, v_l, e_v, v_v are the quantities at saturation, $v = 1/\rho$ and x is the vapor quality, expressed as in the HEM frame

$$x = \frac{h - h_l}{h_g - h_l}, \tag{6}$$

where the specific enthalpy h is written as $h = e + pv$.

The wave propagation speed is an intrinsic characteristic of hyberpolic system of equations. However, in order to solve the system numerically, the wave propagation speed is often assumed to be equal to the speed of sound of the material, which can be estimated by thermodynamic variables. Here, the two-phase speed of sound of the HEM is written as: (De Lorenzo et al., 2017)

$$c^2 = \frac{\frac{p}{\rho} - \rho\left(\frac{\partial e}{\partial \rho}\right)_p}{\rho\left(\frac{\partial e}{\partial p}\right)_\rho}. \tag{7}$$

Due to the nature of the HEM model, it estimates the lowest speed of sound comparing to non-equilibrium models. This two-phase speed of sound is compared to other formulations of two-phase speed of sound for CO_2 in (Fang et al., 2018). Two discontinuities are observed across the saturation line on the liquid and vapor sides. This characteristic of the HEM has been discussed by Nakagawa et al. (2009a) and Flåtten and Lund (2012).

2.2. Density-based solver

The *rhoCentralFoam* solver is a density-based solver, which is originally designed for simulations of high-speed compressible flows. The density, velocity and internal energy are solved by the equations of conservation of mass, momentum and energy, respectively. The pressure is computed by the EoS, as it depends simultaneously on density and temperature (though it could be also defined by two other independent thermodynamic variables). The original *rhoCentralFoam* solver was implemented by Greenshields et al. (2010) in the OpenFOAM library. It is based on a finite volume method using semi-discrete, non-staggered central schemes for collocated variables. It is a Riemann-solver-free approach to capture the discontinuities in compresssible flows, such as shock waves or contact surfaces. This solver compares fairly well to more complex methods involving Riemann solver, characteristic decomposition or Jacobian evaluation (e.g. monotonous upstream-centered scheme for conservation laws (van Leer, 1979), essential non-oscillatory (ENO) schemes (Harten et al., 1987)...).

The Navier–Stokes equations are considered as the governing equations in the present case. The viscous terms, $\nabla\cdot\mathbf{T}$ and $\nabla\cdot(\mathbf{T}\cdot\mathbf{u}) + \nabla\cdot\mathbf{j}$ are added to the right-hand side (RHS) of Eq. (2) and Eq. (3), respectively. $\mathbf{T}$ is the stress tensor assuming a zero bulk viscosity:

$$\mathbf{T} = 2\mu * \mathrm{dev}(\mathbf{D}), \tag{8}$$

where μ is the dynamic viscosity and $\mathbf{D}$ denotes the deformation gradient tensor, $\mathbf{D} = \frac{1}{2}(\nabla\mathbf{u} + \nabla\mathbf{u}^T)$. Its deviatoric component is $\mathrm{dev}(\mathbf{D}) = \mathbf{D} - \frac{1}{3}\mathrm{tr}(\mathbf{D})\mathbf{I}$, where $\mathbf{I}$ is the unit tensor. The heat diffusion is presented by Fourier's Law:

$$\mathbf{j} = -k\nabla\mathbf{T}, \tag{9}$$

where k is the thermal conductivity. In practice, temperature T is transformed to the internal energy in the solver to respect its conservative formulation.

A first-order Euler implicit scheme is employed for the temporal discretization. The Kurganov and Tadmor (KT) or Kurganov, Noelle and Petrova (KNP) schemes (Kurganov et al., 2001; Kurganov and Tadmor, 2001) are considered for the spatial discretization. They are both second-order semi-discrete, non-staggered schemes and the KNP is considered for the following simulations. For example, the convective terms, such as $\nabla[\mathbf{u}\rho]$, $\nabla[\mathbf{u}(\rho\mathbf{u})]$, $\nabla[\mathbf{u}(\mathbf{u}\rho E)]$, and $\nabla[\mathbf{u}(\mathbf{u}p)]$ are transformed from the volume integration to the surface integration over a control volume by using the Gauss's theorem:

$$\int_V \nabla\cdot[\mathbf{u}\boldsymbol{\Psi}]dV = \int_S [\mathbf{u}\boldsymbol{\Psi}]d\mathbf{S} \approx \sum_f \phi_f \boldsymbol{\Psi}_f, \tag{10}$$

where Σ_f represents the summation over all surfaces of the control volume and ϕ_f is a volumetric flux at the surface defined as $\phi_f = \mathbf{S}_f\mathbf{u}_f$. $\boldsymbol{\Psi}$ denotes the convected variables, such as ρ, $\rho\mathbf{u}$, ρE, and p. The summation of all fluxes over the interface is computed by inward and outward fluxes at the interface combined with a weight factor and writes as

$$\sum_f \phi_f\boldsymbol{\Psi}_f = \sum_f [\alpha\phi_{f+}\boldsymbol{\Psi}_{f+} + (1-\alpha)\phi_{f-}\boldsymbol{\Psi}_{f-} + \omega_f(\boldsymbol{\Psi}_{f+} - \boldsymbol{\Psi}_{f-})], \tag{11}$$

where the weight factor α is fixed to 0.5 for the KT scheme which is considered as a *central* scheme, while the KNP scheme is biased in the upwind direction which depends on one-sided local speed of sound. The third term on the RHS of Eq. (11) represents a diffusion term weighted by a volumetric flux ω_f, which depends on the maximum propagation speed of the discontinuities. The detailed formulations are found in (Greenshields et al., 2010). The inward and outward fluxes at the interface are determined based on the cell-centered values by interpolating methods in the OpenFOAM library, such as the upwind, Minmod (Roe, 1986) or van Leer (van Leer, 1974) interpolations. The gradient terms, such as the pressure gradient, are constructed in a similar way by the weighted inward and outward fluxes. The Laplacian terms for the viscous force are split into orthogonal and non-orthogonal parts, which is suitable when using polyhedral meshes.

The equations are solved sequentially by the solver. The procedure can be summarized as follows:

- Construct interface fluxes by interpolating the conservative variables, $\mathbf{U}^n$, at the previous time step with limiters.
- Solve the density equation to obtain ρ^{n+1}.
- Solve the inviscid momentum equation to obtain ρu^{n+1}.
- Solve the diffusion equation for the velocity to update u^{n+1}.
- Solve the inviscid energy equation to obtain ρE^{n+1}.
- Solve the diffusion equation for the internal energy to update e.
- Update the conservative variables at boundaries.

2.3. Bulk viscosity

The bulk viscosity κ is usually set equal to zero according to the Stokes' hypothesis:

$$\kappa = \lambda + \frac{2}{3}\mu = 0, \tag{12}$$

with λ the second coefficient of the viscosity and μ the dynamic viscosity. This hypothesis is valid for mono-atomic gases. However, it was revealed that for some polyatomic gases, such as CO_2, the bulk viscosity may become important. The viscosity ratio κ/μ can reach indeed 10^3 at ambient temperature, which could have a significant impact on the numerical modelling (Cramer, 2012; Emanuel, 1992; Tisza, 1941). Physically, the bulk viscosity is due to the relaxation of internal degrees of freedom such as vibrational and rotational degrees of freedom. It can be measured

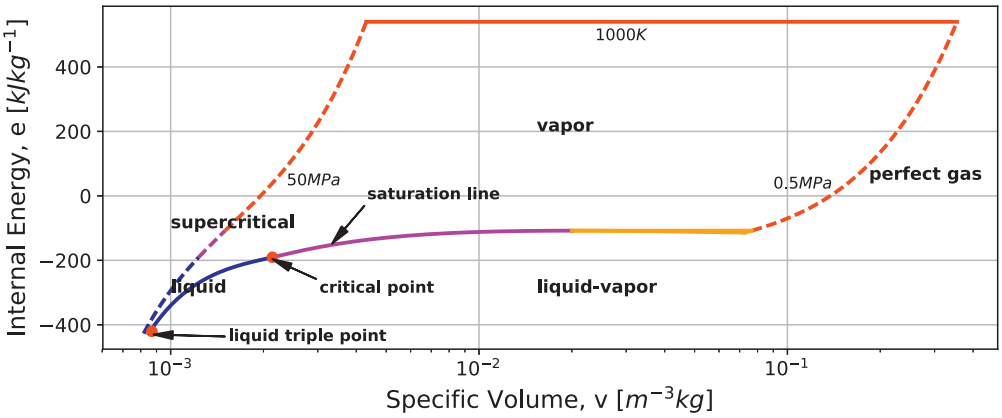

Fig. 1. Entire range of the tabulated EoS in the $e-v$ diagram.

experimentally by supersonic absorption (Tisza, 1941). The general form of the stress tensor writes:

$$\mathbf{T} = \lambda(\nabla \cdot \mathbf{u})\mathbf{I} + \mu[\nabla\mathbf{u} + (\nabla\mathbf{u})^T]. \tag{13}$$

If the flow is incompressible, the first term on the RHS of Eq. (13) is equal to zero. If the flow is compressible, the stress tensor can be rewritten as:

$$\mathbf{T} = \mu\nabla\mathbf{u} + \mu\left[\nabla\mathbf{u}^T - \frac{2}{3}tr(\nabla \cdot \mathbf{u})\mathbf{I}\right] + \kappa\, tr(\nabla \cdot \mathbf{u})\mathbf{I}, \tag{14}$$

where tr represents the trace of the matrix. If the bulk viscosity is set to zero, Eq. (14) simplifies to Eq. (8). It can be seen that the stress tensor is separated into three parts: the orthogonal, non-orthogonal and bulk viscosity parts. It is also noticed that the bulk viscosity part has only diagonal contributions, which provides a second-order correction to the pressure prediction, arising as a consequence of both compression and dilatation. The main difficulty remains to accurately determine the bulk viscosity. Only very limited experimental data have been reported in the literature and the results are highly dependant on the characteristic of the measurement technique (Jaeger et al., 2018). In this study, a simple formulation derived by Zuckerwar and Ash (2006) from Chapman and Cowling (1970)'s formulation is used:

$$\kappa = \frac{2(d-3)}{d^2}P\tau, \tag{15}$$

where d is the number of molecular degrees of freedom ($d = 5$ for CO_2 according to Zuckerwar and Ash, 2006), P denotes the pressure and τ indicates the relaxation time. It should be mentioned that there is currently no reference to fix the relaxation time for CO_2. Its influence will be then discussed in the following sections.

2.4. Real gas approach

An accurate and efficient look-up table method has been developed and validated for CO_2 (Fang et al., 2018) based on the works of De Lorenzo et al. (2017) and Kunick et al. (2008). The original Span–Wagner EoS (Span and Wagner, 1994), which is considered as the standard EoS for CO_2, is tabulated. The Refprop (Lemmon et al., 2010) and Coolprop (Bell et al., 2014) database equally rely on it for CO_2 properties. This tabulated approach is designed for the conservative formulation, where the density and the internal energy are considered as two independent variables. Therefore, the rest of thermodynamic properties can be computed directly without any iterative inversion process. In Fig. 1, the range of the tabulated approach is shown on an $e-v$ diagram, for temperatures from 216.59 K (the triple point temperature) to 1000 K and pressures up to 50 MPa. The details and validation of this method in terms of accuracy and efficiency may be found in (Fang et al., 2018). Additionally, the transport properties, such as the dynamic viscosity and the thermal conductivity, are implemented as separated equations depending on density and temperature (Harvey, 2016; Huber et al., 2016; Vesovic et al., 1989). It is noted that the viscosity of the two-phase mixture is based on the mass averaged value (Cicchitti et al., 1960):

$$\mu_m = x\,\mu_g + (1-x)\,\mu_l, \tag{16}$$

where x denotes the vapor quality, μ_m, μ_g and μ_l denote the mixture, vapor, and liquid dynamic viscosities. Other mixing laws used to determine the two-phase viscosity can be easily evaluated, such as McAdams et al. (1942), Beattie and Whalley (1982), or Fourar and Bories (1995). The thermal conductivity of CO_2 in its different states is computed based on the experimental data of Vesovic et al. (1989) and a mixing law is also used to determine the conductivity of the two-phase mixture similarly to the dynamic viscosity (Eq. (16)).

During the solving procedure, thermodynamic variables (e.g. the pressure, speed of sound, temperature, dynamic viscosity,and isobaric heat capacity) at the center of cells are computed by using the density and the internal energy at the same cell. This in-house tabulated approach was developed in Fortran language. Practically, it is wrapped as an external static library in the C++-based *rhoCentralFoam* solver.

2.5. NSCBC boundary condition

The basic Dirichlet and Neumann type boundary conditions are available in the OpenFOAM library. However, they are not sufficient for compressible flows. For an hyperbolic system of equations, the most appropriate way to manipulate the inlet and outlet boundary conditions is indeed by using characteristic variables. Fixing directly the characteristic variables at the boundary can generate non-physical spurious waves, which can affect the accuracy and the numerical stability of the solver. Therefore, a special treatment for open boundary conditions (i.e. outlet) is required. This kind of issue has been extensively investigated for the high resolution of compressible flows (e.g. through Large-eddy (LES) and Direct numerical (DNS) simulations) (Fosso et al., 2012; Poinsot and Lele, 1992; Yoo and Im, 2007). In the present solver, the Navier–Stokes characteristic boundary condition (NSCBC) is implemented based on the former works of (Fosso et al., 2012; Poinsot and Lele, 1992) and coupled to the tabulated EoS. Primarily, one focuses on the outlet boundary condition as illustrated in Fig. 2. Navier–Stokes equations in their characteristic form following the x-direction may

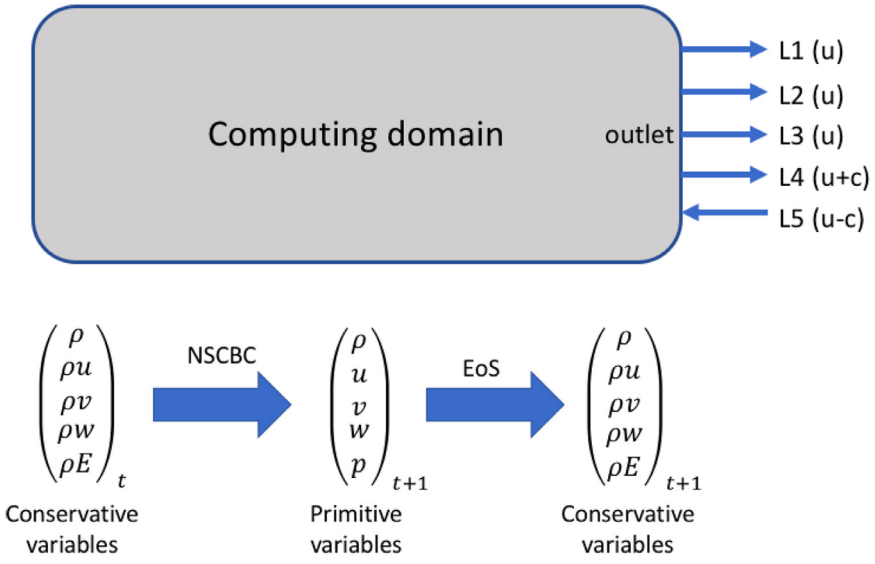

Fig. 2. Scheme displaying the incoming and outgoing waves at the outlet boundary and the procedure to compute corrected boundary variables.

be written as (Fosso et al., 2012):

$$\begin{bmatrix} c^2\frac{\partial \rho}{\partial t} - \frac{\partial p}{\partial t} \\ \frac{\partial v}{\partial t} \\ \frac{\partial w}{\partial t} \\ \frac{\partial p}{\partial t} + \rho c \frac{\partial u}{\partial t} \\ \frac{\partial p}{\partial t} - \rho c \frac{\partial u}{\partial t} \end{bmatrix} + \begin{bmatrix} c^2 L_1 \\ L_2 \\ L_3 \\ \rho c L_4 \\ \rho c L_5 \end{bmatrix} + \begin{bmatrix} T_1 \\ T_2 \\ T_3 \\ T_4 \\ T_5 \end{bmatrix} + \begin{bmatrix} D_1 \\ D_2 \\ D_3 \\ D_4 \\ D_5 \end{bmatrix} = \begin{bmatrix} 0 \\ 0 \\ 0 \\ 0 \\ 0 \end{bmatrix}, \tag{17}$$

where T_i denotes the transverse terms, D_i represents the diffusion terms, and L_i is the vector of the characteristic wave amplitude. It writes

$$L = \begin{bmatrix} u\left[\frac{\partial \rho}{\partial x} - \frac{1}{c^2}\frac{\partial p}{\partial x}\right] \\ u\left[\frac{\partial v}{\partial x}\right] \\ u\left[\frac{\partial w}{\partial x}\right] \\ (u+c)\left[\frac{\partial u}{\partial x} - \frac{1}{\rho c}\frac{\partial p}{\partial x}\right] \\ (u-c)\left[-\frac{\partial u}{\partial x} - \frac{1}{\rho c}\frac{\partial p}{\partial x}\right] \end{bmatrix}. \tag{18}$$

Depending on the sign of the propagation speed $(u, u+c, u-c)$, the characteristic waves can be defined as incoming or outgoing waves. Outgoing waves are computed using interior information with an one-sided scheme, while the incoming waves are determined by the physical information available at the boundary (i.e. the outlet pressure). Here, one assumes that the outflow is along the x-direction only. The transverse and viscous terms are neglected. At the outlet, the flow is indeed usually unidirectional or a sponge layer is often added for stabilizing the simulation, such that the transversal contribution has a negligible effect. Moreover, for a fully turbulent flow, viscous effects can be neglected as well. Regarding a subsonic pressure outlet boundary condition, L_5 is the only incoming wave. Hence, L_1, L_2, L_3, L_4 are evaluated by values available in the computational domain. Poinsot and Lele (1992) proposed the following equation to evaluate L_5:

$$L_5 = K * (p - p_{tar}), \tag{19}$$

where p is the instantaneous pressure at the boundary, while p_{tar} is the target pressure which is fixed at the boundary. K is a relaxation coefficient defined as $K = \sigma c \frac{1-M_{max}^2}{l}$, where $\sigma = 0.25$, M_{max} denotes the maximum Mach number at the boundary and l is a characteristic length, fixed here to the nozzle's length.

As shown in Fig. 2, by solving Eq. (17), one can obtain the corrected values of ρ, u, v, w, p for the next time step. However, the resolved variables at the boundary are conservative variables, ρ, ρu, ρv, ρw, and ρE. Therefore, the corrected conservative variables are computed by the corrected primitive variables through the EoS. Noting that if the Mach number is higher than one at the boundary, this subsonic pressure outlet boundary condition switches to the supersonic outlet boundary condition in which all information come from the interior of the computational domain.

Two validation cases are presented in the next section: first one is to assess the density-based solver, the second one is to evaluate NSCBC at the outlet boundary.

3. Validation of the flow solver

3.1. Configuration 1: the shock tube

The shock tube problem is simulated by applying the modified *rhoCentralFoam* solver in order to evaluate the capture of discontinuities (e.g. shock waves, expansion waves, and contact surfaces) in compressible flows. Initially, a discontinuity is created in the middle of the tube, by imposing $p_L = 3$ MPa, $T_L = 300$ K and $\rho_L = 63.376$ kg.m^{-3} at rest for the left part and $p_R = 1$ MPa, $T_R = 300$ K and $\rho_R = 18.579$ kg.m^{-3} at rest for the right part. As a result, the CO_2 flow is driven by the pressure difference from left to right. A shock wave forms and propagates to the right of the tube, while expansion waves are generated and propagate to the left. A contact surface is created as well, which can be observed on Fig. 3 from the density profile. The 1D tube is meshed with 1000 regularly spaced nodes. The time step is computed at each time step to guarantee that the Courant–Friedrich–Levy (CFL) number remains smaller than 0.2. Viscous effects are neglected, such that the code solves the Euler equations. The Van Leer interpolation is used to compute the variables at the cell-interface. The

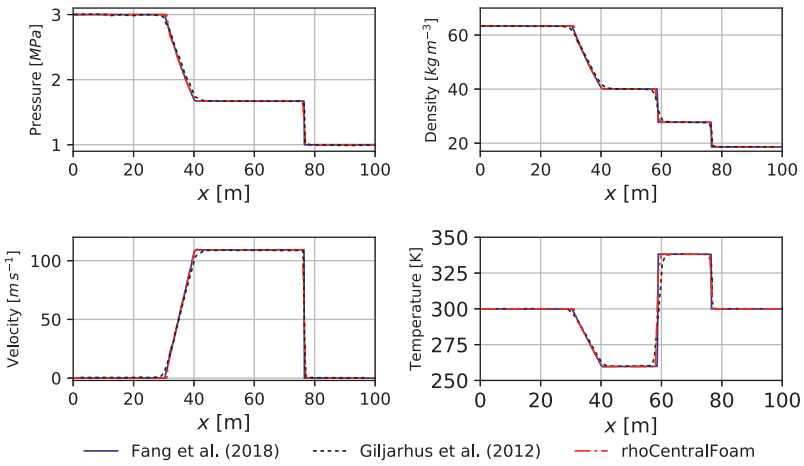

Fig. 3. Pressure, density, velocity and temperature profiles at $t = 0.08$ s for the shock tube problem.

present results are compared to those of Fang et al. (2018) and Giljarhus et al. (2012). The results of Fang et al. (2018) are based on the CLAWPACK solver (LeVeque, 2002; LeVeque and Berger, 2017) which uses the Godunov approach combining HLLC Riemann solver (Toro, 1997; Toro et al., 1994). Giljarhus et al. (2012) conducted the simulation using the MultiSTage Approach (MUSTA), which is also a Riemann-solver-free approach (Titarev and Toro, 2005). The comparison is shown in Fig. 3. A good agreement is obtained among these three simulations. Only some weak discrepancies can be observed at the discontinuities, which come from the numerical dissipation. It is noted that *rhoCentralFoam* solver is less accurate than the CLAWPACK solver, but more accurate than the MUSTA. This case was also simulated by the pressure-based solver and density-based solver using ANSYS Fluent (not presented here for sake of brevity). The SIMPLEC and COUPLED schemes with PRESTO! and a second-order spatial discretization scheme for the pressure have been also evaluated. It was found that in order to capture correctly the shock waves, contact surface and expansion waves, the pressure must be discretized by at least a second-order accurate scheme. Otherwise noticeable numerical oscillations appear at the locations of the contact surface and the shock waves. Hence, the pressure-based solver is less suitable than the density-based solver for compressible flows.

3.2. Configuration 2: depressurization

The depressurization is a classic scenario of the flashing phenomenon. Hence, it was chosen to validate the HEM and meanwhile to evaluate the NSCBC at the outlet boundary. A 100-meter tube was filled with CO_2 at $p = 10$ MPa and $T = 300$ K (supercritical state). At the initial time, the right side of the tube is opened to the ambient with pressure at 3 MPa. The discontinuities are generated and propagate toward the left side of the tube. A 1000-node mesh is used associated with a maximum CFL number equal to 0.2. The profiles of pressure, temperature and speed of sound at $t = 0.2$ s are shown in Fig. 4. Two discontinuities can be observed for the pressure profile. The left one is the expansion wave of the supercritical CO_2, while the right one is the evaporation front where the CO_2 vapor is created. The present results are compared to those of Hammer et al. (2013) and Fang et al. (2018). A second-order accurate MUSCL-FORCE scheme was used by Hammer et al. (2013), whereas the upwind interpolation was used in *rhoCentralFoam* solver. The differences are located at the discontinuities. *rhoCentralFoam* provides similar results compared to the MUSCL-FORCE scheme, while being more dissipative than the CLAWPACK solver. In this simulation, the upwind interpolation

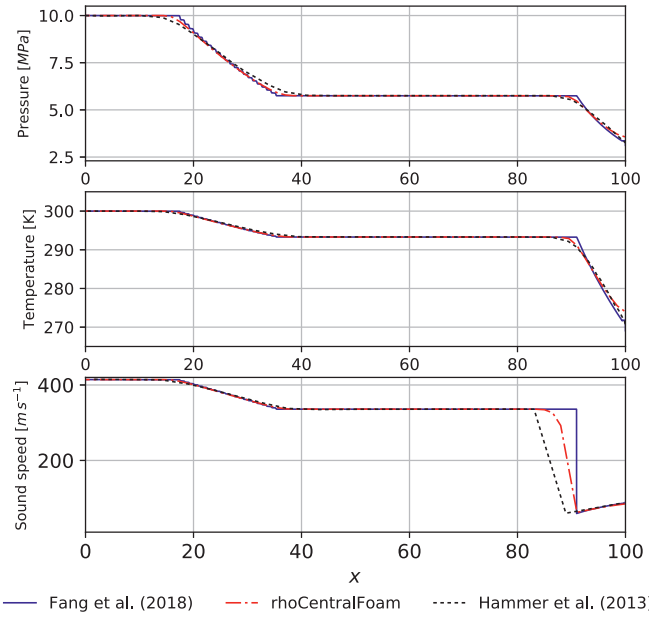

Fig. 4. Comparisons between the present solver and the numerical results of Fang et al. (2018) and Hammer et al. (2013) in terms of pressure, temperature and liquid mass fraction distributions in the streamwise direction at $t = 0.2$ s.

instead of the Van Leer interpolation is used to construct the surface fluxes (inward and outward fluxes in Eq. (11)). It is more dissipative at the discontinuity but it can insure the stability of the simulation.

4. Converging-diverging Laval nozzles

4.1. Simulation set-up

Two converging-diverging nozzles are simulated in 2D plan-symmetric corresponding to the experimental set-ups developed by Nakagawa et al. (2009b). The semi-dimension parameters are shown in Table 1, where d_{in} and d_{out} denote the semi-heights at the inlet and the outlet of the nozzle, l_c and l_d represent the lengths of the converging and diverging parts, respectively. h_t is the semi-height at the throat, while d_w is the thickness of the rectangular nozzle. The two nozzles differ only in terms of their diverging angle θ.

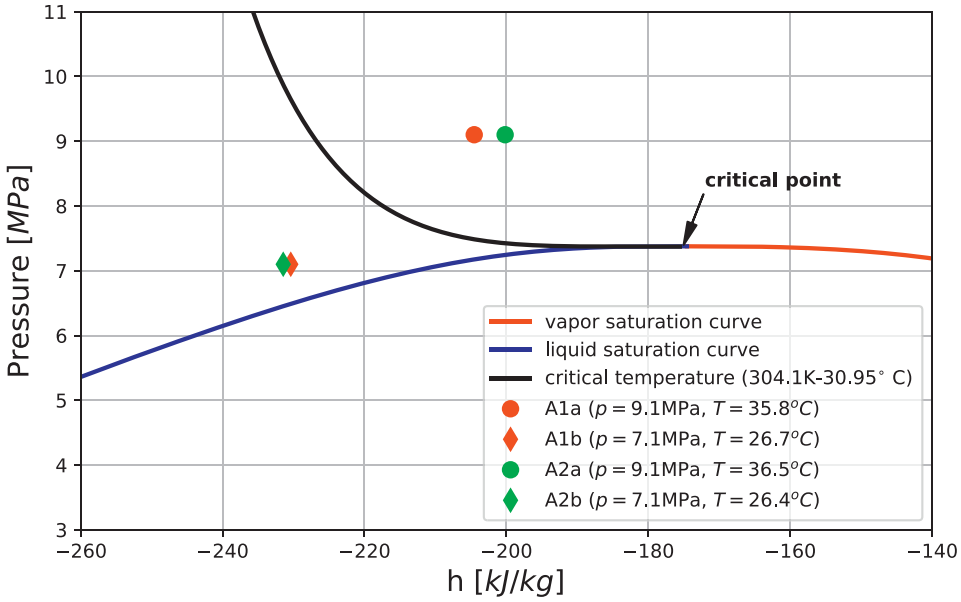

Fig. 5. Considered operating conditions for the A1 and A2 nozzles represented on a $p-h$ diagram.

Table 1
Geometric parameters of the nozzles.

Nozzle	d_{in} (mm)	l_c(mm)	h_t (mm)	l_d(mm)	$\theta[^o]$	d_{out}(mm)	d_w(mm)
A1	5	27.35	0.12	56.15	0.306	0.42	3
A2	5	27.35	0.12	56.15	0.612	0.72	3

Table 2
Boundary conditions for the Laval nozzle simulations.

Case	$P_{in}[MPa]$	$T_{in}[K]$	Outlet	Top wall	Bottom wall	Lateral walls
A1a	9.1	308.95	Supersonic	Non-slip	Symmetry	Empty
A1b	7.1	299.85	Supersonic	Non-slip	Symmetry	Empty
A2a	9.1	309.65	Supersonic	Non-slip	Symmetry	Empty
A2b	7.1	299.55	Supersonic	Non-slip	Symmetry	Empty

Supercritical and subcritical operating conditions are simulated for each nozzle. According to the experimental measurements, there is no shock wave appearing within these two nozzles. Therefore, the supersonic outlet boundary condition is used, in which all variables at the boundary are computed by using the interior information. The boundary conditions are summarized in Table 2. At the inlet, the pressure and temperature are imposed, whereas the top wall is set to a no-slip condition. The bottom wall is considered as the symmetric plan. The term “empty” used for the lateral walls refers to the case for which the equations are not solved in that direction. It is a proper method inherent to the OpenFOAM library to perform 2D simulations. The operating conditions at the nozzle inlet are displayed on the $p-h$ diagram, in Fig. 5. It can be observed that the A1 and A2 nozzles operate almost at the same operating conditions for the supercritical case as well as for the subcritical case. The structured mesh is generated by Gmsh (Geuzaine and Remacle, 2009) and consists of $11,514$ cells. The grid convergence has been carefully checked by considering 3 mesh grids composed of $11,514$, $24,804$, and $48,032$ elements, respectively.

The Kurganov approach is used to compute the interface fluxes and the Van Leer interpolation method is considered to interpolate variables from the cell center to the surface. A first-order Euler implicit scheme is used for the temporal discretization together with the least square method to compute gradient terms at the interfaces. The Gauss linear method is applied for the divergence and Laplacian terms at the interfaces. The “Gauss–Seidel” smooth solver is enabled to solve implicitly the diffusion equation. The *rhoCentralFoam* solver is an unsteady solver. Hence, the steady state is considered to be achieved when the difference in terms of mass flow rates between the inlet and the outlet remains below 0.5%.

4.2. 2D numerical results

First of all, it is noteworthy that all calculations have also been performed in 3D. As absolutely no difference was observed between the 2D and 3D calculations, all the results presented hereafter have been obtained by 2D symmetric simulations. Moreover, the mixing laws proposed by McAdams et al. (1942), Beattie and Whalley (1982), Fourar and Bories (1995) to evaluate the two-phase viscosity have also been compared here leading here to undistinguishable results. These comparisons are not shown here for sake of brevity. Note also that all the streamwise profiles displayed in this section are extracted on the symmetry axis at $y=0$. The values at the wall and on the symmetry axis have been verified and no difference has been noticed. The 2D calculations in this section are performed through Mammouth Parallel 2bs cluster which consists of 1096 nodes in total at Universit de Sherbrooke. Each node has 24 CPUs with 31 GB of memory. The computational time is about 40 h with 24 CPUs running in parallel.

The pressure distributions for nozzles A1 and A2 under supercritical conditions are shown in Fig. 6(a) and Fig. 6(b), respectively. In Fig. 6(a), the present numerical results (the solid black curve) are compared with Angielczyk et al. (2010) (the blue dotted curve) computed by a 1D HRM. For the HRM, the flashing starts just before the throat, while the present solver based on the HEM predicts the flashing when saturation conditions are met right at the throat. The experimental pressure measurements (the red diamonds) and the saturation pressures computed by the temperature measurements (the white squares) are also displayed in Fig. 6(a). The HRM predicts slightly better the pressure profile near the throat than the present model. However, regarding the experimental results, the measured pressure is very close to the computed saturation pressure, which indeed confirms the thermodynamic equilibrium assumption. Hence, it can not ensure that the HRM is more appropriate in the present case. Concerning the present results (HEM), relatively larger discrepancies are found right after the throat, whereas a good agreement is obtained at the nozzle outlet. These

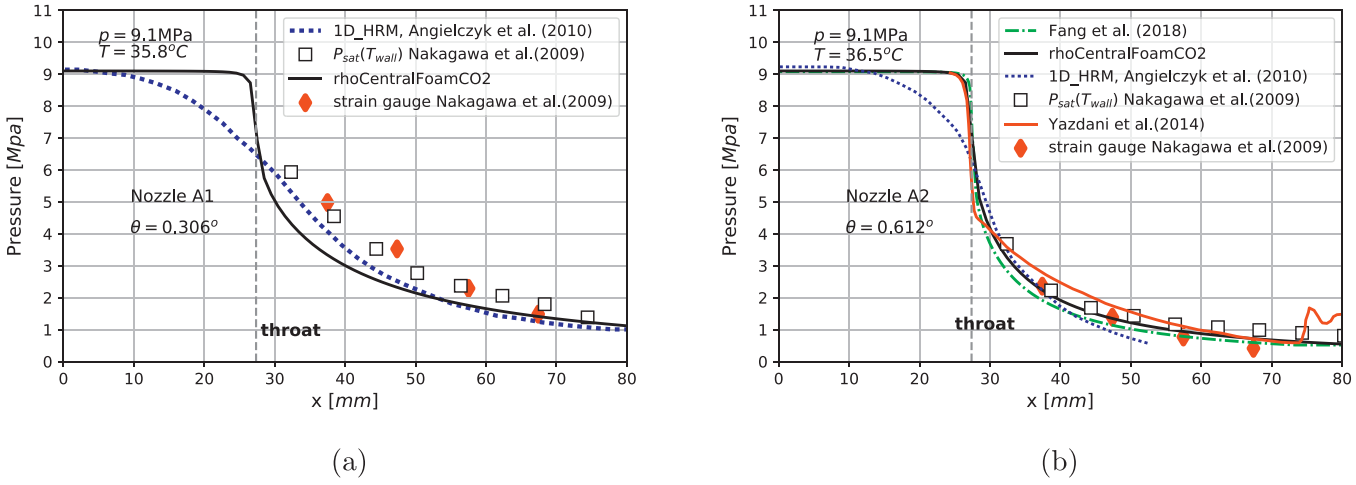

Fig. 6. Pressure profiles for nozzles A1 and A2 under supercritical operating conditions. Comparisons with the experimental data of Nakagawa et al. (2009b), the 1D HRM of Angielczyk et al. (2010), the CLAWPACK solver used by Fang et al. (2018) and the two-phase model of Yazdani et al. (2014). (For interpretation of the references to color in this figure, the reader is referred to the web version of this article.)

differences could be explained by turbulence or bulk viscosity effects, which will be considered hereafter. Besides, considering the very low diameter of the throat (0.24 mm), if the measurement volume has a comparable dimension, it could have a non-negligible effect on the measurement accuracy.

A good agreement in terms of pressure distribution is obtained for case A2a. The nozzle A2 has a larger diverging angle and operates equally under supercritical conditions. In Fig. 6(b), Angielczyk et al. (2010) results (the blue dotted curve) stop at the middle of the diverging part because of the presence of the solid phase due to a overestimate expansion rate. On the contrary, the present results continue up to the outlet and agree perfectly with the experimental results. Furthermore, the present results are compared to those computed by the CLAWPACK solver (Fang et al., 2018) (the green dash-dot curve). Some small discrepancies are observed near the throat. Here, the differences are due to viscous effects, because the CLAWPACK solver considers only the inviscid Euler equations, while the present solver solves the Navier–Stokes equations. The two-phase model of Yazdani et al. (2014) (red line), which includes real-fluid properties of CO_2, local mass and energy transfer between phases, and a two-phase sonic velocity model, is also displayed and some differences appear mainly located in the middle of the diverging part. Some oscillations are also observed around the outlet, which may be attributed to an inappropriate outlet boundary condition. Even though the pressure profiles are similar between the present simulation and those of Yazdani et al. (2014), the vapor volume fraction, the Mach number, and the streamwise velocity in the diverging part are totally different (see Fig. 4 in (Yazdani et al., 2014)). In the present simulation, the vapor creates at the throat and the quality has a quasi flat profile at each cross section, while in Yazdani et al. (2014), the vapor creates primarily near the wall and the vapor quality is minimum at the center of each cross section. It is besides surprising that in Yazdani et al. (2014), the flow firstly becomes supersonic near the wall then at the center of the nozzle.

Fig. 7(a) and Fig. 7(b) illustrate the pressure profiles under subcritical conditions for both nozzles. A good agreement is still obtained for the nozzle A2, while for the nozzle A1, the pressure agrees better near the outlet than close to the throat. An abrupt change in the experimental pressure profile can be observed between second and third points in the diverging part. Hence, the uncertainty of the experimental measurement should be also considered. Unfortunately uncertainties of experimental measurement is not reported in Nakagawa et al. (2009b). As mentioned previously about Yazdani et al. (2014)'s simulation, even though the pressure profile is identical, the flow features could be different.

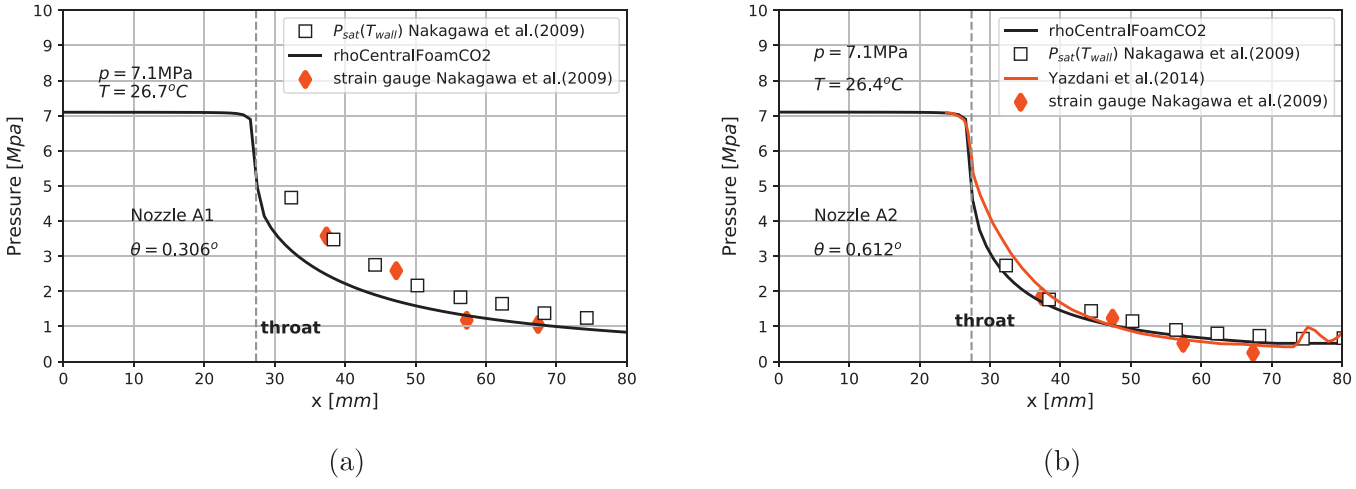

Fig. 7. Pressure profiles for nozzles A1 and A2 under subcritical operating conditions. Comparisons with the experimental data of Nakagawa et al. (2009b) and the two-phase model of Yazdani et al. (2014).

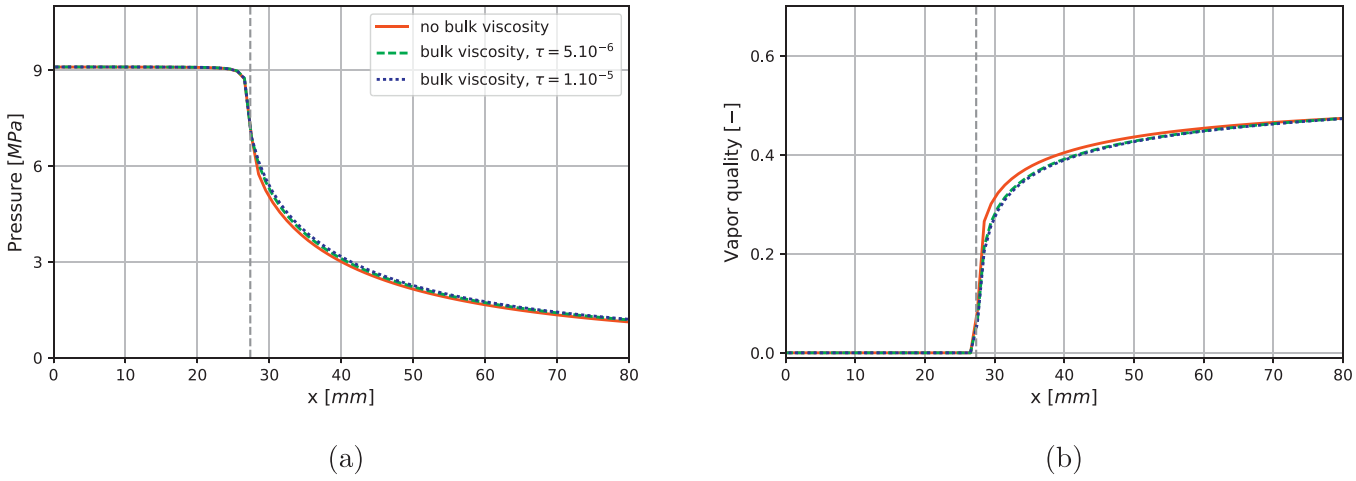

Fig. 8. Pressure and vapor quality distributions along the streamwise direction for nozzle A1 under supercritical conditions. The red solid line presents the results without considering the bulk viscosity. The green dashed line and blue dotted line present the results with bulk viscosity and $\tau = 5 \times 10^{-6}$ and $\tau = 10^{-5}$, respectively. (For interpretation of the references to color in this figure legend, the reader is referred to the web version of this article.)

Table 3
The maximum discrepancies between numerical results and experimental results in different cases.

Cases	Max diff to measured pressures (%)	Max diff to saturated pressures (%)
A1a supercritical	34	27.6
A1b subcritical	31	33
A2a supercritical	14	16
A2b subcritical	17	11

Hence, more experimental measures are required, such as the velocity, the mass flow rate, the visualisation of the density gradient and the vapor quality. Furthermore, the accuracy of the present model is surprisingly not related to the operating condition (whatever supercritical or subcritical), but it seems to be related only to the nozzle geometry itself. The maximum discrepancies between numerical results and experimental results are summarized in Table 3 for different cases. The measured pressures are presented by the red square in the original figures, while the saturated pressures are presented by the white squares. It can be seen that for the nozzle A, under the supercritical and subcritical conditions, the discrepancies are both larger than those for the nozzle B.

4.3. Influence of the bulk viscosity

The bulk viscosity is considered in the simulation of the nozzle A1 under supercritical conditions. Two values of the relaxation time have been considered so far: $\tau = 10^{-5}$ and $\tau = 5 \times 10^{-6}$. Note that, for $\tau \geq 10^{-5}$, numerical instabilities arise. Fig. 8 displays the corresponding pressure and vapor quality profiles.

A slight difference in terms of pressure and vapor quality can be observed near the throat. This is due to a difference in expansion rates beyond the throat. However, it does not change the location of the flashing. It can be concluded that the bulk viscosity has no noticeable effect on the flow in a supersonic converging-diverging nozzle for CO_2. However, it should be noted that if a strong compression or expansion occurs, e.g. shock waves, more significant effects could be encountered.

4.4. Influence of the turbulence closure

Reynolds-averaged Navier–Stokes (RANS) simulations have been carried out for nozzle A1 under supercritical conditions. The realizable $k-\varepsilon$ model with standard wall functions and the $k-\omega$ SST model are compared. A 2D structured mesh composed of 89,072 elements is used for the realizable $k-\varepsilon$ model, which implies a maximum wall coordinate y^+ around 65. For this mesh, the computational time is about 63 hours with 40 CPUs using the Niagaras Cluster of Compute Canada consisting of 1500 nodes, each with 40 Intel Skylake cores and 202 GB of memory. The "LowRe-Wallfunction" was set for the turbulence characteristic variables, namely ε and k, at the wall boundary, supporting then that y^+ may be in the buffer layer. The k-ω SST model is associated with a structured mesh composed of 926,054 elements to guarantee that the maximum of y^+ remains smaller than 1, to fully solve the wall boundary layers.It takes about 690 h with 480 CPUs using the Mammouth Parallel 2bs Cluster of Compute Canada. The detail of the meshes are presented in Fig. 9. It can be seen that in order to obtain $y^+ < 1$, the region close to wall is extremely refined. The numerical set-ups for simulations applying $k-\omega$ SST model and $k-\varepsilon$ model are shown in Fig. 4. Fig. 10(a) displays the pressure profiles obtained by the realizable k-ε and k-ω SST turbulence models. The measurements of Nakagawa et al. (2008) are also equally presented. It can be seen that the k-ω SST improves significantly the predictions of the realizable k-ε. The pressure distribution agrees particularly well with the experimental measurements after the throat, whereas the realizable k-ε model provides the same profile as the laminar model previously discussed, underestimating the pressure along the diverging part. To explain that, one should recall that the k-ω SST is also a two-equation eddy-viscosity model, which combines a k-ω formulation in the inner parts of the boundary layer and a standard k-ε in the

Table 4
Numerical set-up for simulations with the $k-\omega$ SST model and the $k-\varepsilon$ model.

Grid element number	Turbulence model	Wall function	y^+	Inlet
89,072	Realizable $k-\varepsilon$	Standard wall functions	≈ 65	5% turbulence intensity
926,054	$k-\omega$ SST	no	< 1	5% turbulence intensity

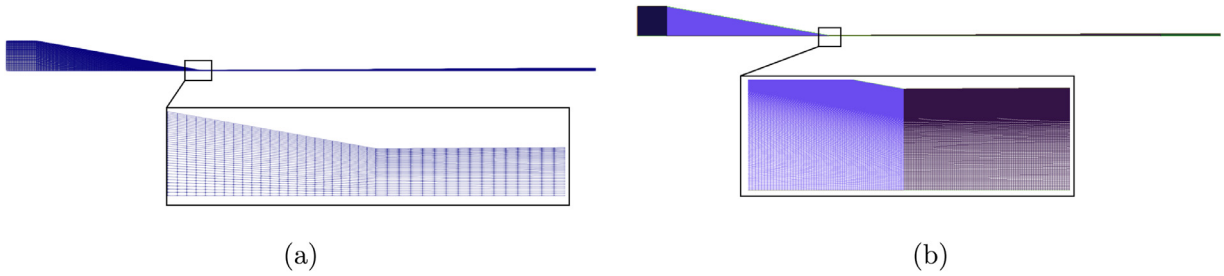

Fig. 9. (a) Mesh used for the simulation with the realizable k-ε model. The y^+ is 65. (b) Mesh used for the simulation applying k-ω SST turbulence model. The y^+ is smaller than 1.

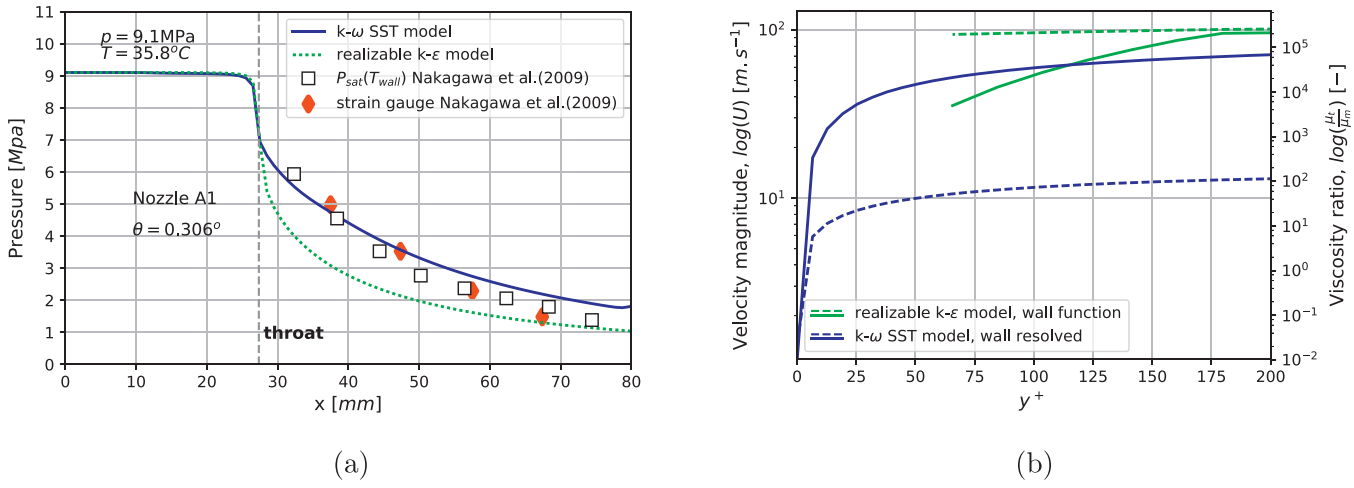

Fig. 10. (a) Streamwise profiles of pressure obtained by the realizable k-ε and k-ω SST turbulence models for nozzle A1 under supercritical conditions. Symbols represent Nakagawa et al. (2008)'s measurements; (b) Vertical profiles of the streamwise velocity (solid lines) and viscosity ratio μ_t/μ_m (dashed lines) at $x = 28$ mm.

bulk region. Saying that, there are two possible explanations for the best behavior of the k-ω SST: (i) it is known to produce too large turbulence intensities in flow regions with strong acceleration but still less than the k-ε model; (ii) it exhibits an inherent low-Reynolds number behavior without damping functions. So it points out the prime importance to well solve the boundary layer development along the wall of diverging part.

In the present case, the flow inside the nozzle is fully turbulent with Reynolds numbers (based on the local diameter, which ranges between 0.2 mm at the throat and 5 mm at the inlet) $\simeq 10^6$. At such a high Reynolds number, the realizable k-ε model overdissipates with a viscosity ratio, μ_t/μ_m around 10^5, whereas μ_t/μ_m for the k-ω SST closure is around 10^2 at this particular streamwise position $x = 28$ mm just after the throat (Fig. 10(b)). μ_t denotes the turbulent viscosity, while μ_m denotes the laminar mixture viscosity. The extremely high numerical dissipation of the realizable k-ε model results in a thicker boundary layer. By conservation of mass, the streamwise velocity close to the symmetry plane is then much higher than the one predicted by the k-ω SST. Thus, it explains the underprediction of the pressure by the realizable k-ε previously observed. Moreover, for Nakagawa nozzles the throat is quite narrow ($h_t = 0.12$ mm). Hence, the boundary layer could occupy a large fraction of the duct and may give a significant effect. It can be seen in Fig. 10(b) that the k-ω SST model predicts a thinner boundary layer than that by the realizable k-ε model. It results in the different pressure distribution in Fig. 10(a). For the simulation applying the realizable k-ε, the wall function is used, which cannot accurately predict the boundary layer for this case. Though using wall functions benefits a significant gain of computation time, it should be carefully validated. Moreover, the subcritical conditions ($p = 6$ MPa and $p = 7$ MPa) of the nozzle A have also been simulated by using $k - \omega$ SST model without wall function. Good agreements have been also obtained.

5. Conclusion

A new flow solver has been developed under the opensource library OpenFOAM for simulating two-phase CO_2 supersonic flows. Compared to most existing solvers, its main ingredients are:

1. A full density based solver suitable to simulate highly compressible flows;
2. The Homogeneous Equilibrium Model (HEM) is used to predict the flashing phenomenon;
3. The CO_2 properties are computed by an accurate and efficient tabulated EoS, which has proven to be up to 67 faster than the underlying Span–Wagner EoS (Fang et al., 2018);
4. The Navier–Stokes Characteristic Boundary Condition (NSCBC) is implemented to insure stable boundary conditions at the outlet of the computational domain;
5. The bulk viscosity is modeled through the Zuckerwar and Ash's (Zuckerwar and Ash, 2006) formulation;
6. Turbulence effects are accounted for by a k-ϵ realizable model with wall functions and a k-ω SST model without wall functions.

Even if more sophisticated two-phase models could be implemented further, it can be considered as a promising tool to investigate two-phase compressible CO_2 flows in ejectors for refrigeration applications. To demonstrate that, two test cases have been first performed, namely the shock tube and depressurization, to validate successively the capture of shock waves and the modeling of the flashing phenomenon. Then, two converging-diverging nozzles

with two different diverging angles have been simulated under supercritical and subcritical operating conditions. Fairly good agreements have been obtained compared to the existing experimental results. The results first revealed the 2D nature of the flow field and the weak influence of the two-phase viscosity model. The effects of the bulk viscosity and turbulence have been then quantified in detail in terms of the pressure distribution. The bulk viscosity does not affect significantly the results for these particular conditions. However, this work demonstrated the prime importance to fully resolve the boundary layers to obtain good pressure/velocity predictions which are key parameters driving exergetic transfers within ejectors. Wall-function based models are then not suited for such applications.

k-ω SST calculations and Large Eddy Simulations (LES) are currently running to model more accurately the turbulent mixing for transcritical CO_2 ejectors. The exergy tube analysis proposed by Lamberts et al. (2017) will be applied to better understand the exergy transfer within this type of ejector.

Acknowledgments

Yu Fang and Sébastien Poncet acknowledge the support of the NSERC chair on industrial energy efficiency established in 2014 at Université de Sherbrooke funded by Hydro-Québec, Natural Resources Canada (CanmetEnergy-Varennes) and Rio Tinto Alcan. Computational resources have been provided by Compute Canada and the Consortium des Équipements de Calcul Intensif (CÉCI), funded by the Fonds de la Recherche Scientifique de Belgique (F.R.S.-FNRS) under Grant no. 2.5020.11.

Appendix A. Nomenclature

Acronyms	
CFCs	ChloroFluoroCarbons
CFD	Computational fluid dynamics
CFL	Courant-Friedrich-Levy
CO_2	Carbon dioxide
DNS	Direct numerical simulation
EERC	Ejector-expansion CO_2 transcritical refrigeration cycle
EoS	Equation of state
ENO	Essential non-oscillatory
FORCE	First ORder CEntral
GWP	Global warming potential
HCFCs	HydroChloroFluoroCarbons
HEM	Homogeneous equilibrium model
HLLC	Harten-Lax-van Leer-Contact
HRM	Homogeneous relaxation model
KT	Kurganov and Tadmor
KNP	Kurganov, Noelle and Petrova
LES	Large Eddy simulation
MUSCL	Monotonic upwind scheme for conservation law
MUSTA	MUlti-STage approach
NSCBC	Navier–Stokes characteristic boundary condition
ODP	Ozone depletion potential
RANS	Reynolds-averaged Navier–Stokes
RHS	Right hand side
RGP	Real gas properties
tr	Trace of the matrix
Symbols	
c	Speed of sound ($m.s^{-1}$)
D	Deformation gradient tensor (s^{-1})
D	Diffusion terms (−)
d	Diameter (mm)
d	Degree of freedom
E	Specific total energy ($J.m^3.kg^{-1}$)
e	Specific internal energy ($J.m^3.kg^{-1}$)
g	Specific Gibbs energy ($J.m^3.kg^{-1}$)
h	Specific enthalpy ($J.m^3.kg^{-1}$)
h	Height (mm)
I	Unit tensor (−)
j	Heat flux ($kg.s^{-3}$)
K	Relaxation coefficient ($m^2.kg^{-1}$)
k	Turbulence kinetic energy ($J.m^3.kg^{-1}$)
L	Vector of characteristic wave amplitude (−)
l	Characteristic length(m)
M	Mach number (−)
p, P	Pressure (Pa)
T	Stress tensor (Pa)
T	Temperature (K)
T	Transverse terms (−)
U	Vector of conservative variables (−)
u	Velocity ($m.s^{-1}$)
v	Specific volume ($m^3.kg^{-1}$)
x	Vapor quality (−)
y^+	Dimensionless wall distance (−)
Greek letter	
α	Weighting factor (−)
α	Void fraction (−)
ϵ	Turbulence dissipation ($J.m^3.kg^{-1}$)
κ	Bulk viscosity (Pa.s)
ϕ	Volumetric flux
μ	Dynamic viscosity (Pa.s)
ν	Kinematic viscosity ($m^2.s^{-1}$)
ω	Diffusive volumetric flux based on the speed of sound
ω	Specific turbulence dissipation rate s^{-1}
τ	Relaxation time (s^{-1})
θ	Diverging angle of the nozzle (°)
$\mathbf{\Psi}$	Convective variables
ρ	Density ($kg.m^{-3}$)
Subscripts	
c	Converging part
d	Diverging part
diff	Diffuser
f	Flux at interfaces
f+	Flow outward direction
f-	Flow inward direction
in	Inlet
L	Left side
l	Liquid phase
m	Mixture phase
max	Maximum value
mix	Mixing chamber
out	Outlet
p	Derivative at constant pressure
R	Right side
sat	Saturation state
tar	Target value
t	Turbulence variables
t	Throat
v	Vapor phase
w	Thickness
ρ	Derivative at constant density
Superscripts	
n	Numbering of the time step

References

Ameli, A., Afzalifar, A., Turunen-Saaresti, T., 2017. Non-equilibrium condensation of supercritical carbon dioxide in a converging-diverging nozzle. In: Proceedings of the International Seminar on Non-Ideal Compressible-Fluid Dynamics for Propulsion & Power, Veranna, Italy.

Angielczyk, W., Bartosiewicz, Y., Butrymowicz, D., Seynhaeve, J.M., 2010. 1D modeling of supersonic carbon dioxide two-phase flow through ejector motive nozzle. In: Proceedings of the 13th International Refrigeration and Air Conditioning Conference, West Lafayette, USA.

ANSYS, 2010. Fluent User's Guide. ANSYS.Inc. Technical Report.

Baer, M.R., Nunziato, J.W., 1986. A two-phase mixture theory for the deflagration–to-detonation transition (DDT) in reactive granular materials. Int. J. Multiph. Flow 12, 861–889.

Beattie, D.R.H., Whalley, P.B., 1982. Simple two-phase frictional pressure drop calculation method. Int. J. Multiph. Flow 8, 83–87.

Bell, I.H., Wronski, J., Quoilin, S., Lemort, V., 2014. Pure and pseudo-pure fluid thermophysical property evaluation and the open-source thermophysical property library coolprop. Ind. Eng. Chem. Res. 53 (6), 2498–2508.

Berana, M.S., Nakagawa, M., Harada, A., 2009. Shock waves in supersonic two-phase flow of CO_2 converging-diverging nozzles. HVAC&R Res. 15, 1080–1098.

Bilicki, Z., Kestin, J., 1990. Physical aspects of the relaxation model in two-phase flow. Proc. R. Soc. Lond. A 428, 379–397.
Chapman, S., Cowling, T.G., 1970. The Mathematical Theory of Uniform Gases. Cambridge University Press, Cambridge, U.K.
Cicchitti, A., Lombaradi, C., Silversti, M., Soldaini, G., Zavattarlli, R., 1960. Two-phase cooling experiments pressure drop heat transfer burnout measurements. Energia Nucleare 7, 407–425.
Colarossi, M., Trask, N., Schmidt, D., Bergander, M., 2012. Multidimensional modelling of condensing two-phase ejector flow. Int. J. Refrig. 35, 290–299.
Cramer, M.S., 2012. Numerical estimates for the bulk viscosity of ideal gases. Phys. Fluids. 24, 066102.
De Lorenzo, M., Lafon, P., Di Matteo, M., Pelanti, M., Seynhaeve, J.M., Bartosiewicz, Y., 2017. Homogeneous two-phase flow models and accurate steam-water table look-up method for fast transient simulations. Int. J. Multiph. Flow. 95, 199–219.
Deng, J.Q., Jiang, P.X., Lu, T., Lu, W., 2007. Particular characteristics of transcritical CO_2 refrigeration cycle with an ejector. Appl. Therm. Eng. 27, 381–388.
Elbel, S., Hrnjak, P., 2008. Experimental validation of a prototype ejector designed to reduce throttling losses encountered in transcritical R744 system operation. Int. J. Refrig. 31, 411–422.
Emanuel, G., 1992. Effect of bulk viscosity on a hypersonic boundary layer. Phys. Fluids. 4, 491–495.
European Parliament and the Council, 2014. Regulation (EU) No 517/2014 of the European Parliament and the Council of 16 April 2014 on fluorinated greenhouse gases and repealing Regulation (EC) No 842/2006. Off. J. Eur. Union 150, 195–230.
Fang, Y., De Lorenzo, M., Lafon, P., Poncet, S., Bartosiewicz, Y., 2018. An accurate and efficient look-up table equation of state for two-phase compressible flow simulations of carbon dioxide. Ind. Eng. Chem. Res. 57, 7676–7691.
Flåtten, T., Lund, H., 2012. Relaxation two-phase flow models and the subcharacteristic conditions. Math. Models Methods Appl. Sci 21, 2374–2407.
Fosso, A.P., Deniau, H., Lamarque, N., Poinsot, T., 2012. Comparison of outflow boundary conditions for subsonic aeroacoustic simulations. Int. J. Numer. Meth. Fl 68, 1207–1233.
Fourar, M., Bories, S., 1995. Experimental study of air-water two-phase flow through a fracture (narrow channel). Int. J. Multiph. Flow 4, 621–637.
Geuzaine, C., Remacle, J.-F., 2009. GMSH: a three-dimensional finite element mesh generator with built-in pre- and post-processing facilities. Int. J. Numer. Methods Eng. 79, 1309–1331.
Giacomelli, F., Mazzelli, F., Milazzo, A., 2018. A novel CFD approach for the computation of r744 flashing nozzles in compressible and metastable conditions. Energy 162, 1092–1105.
Giljarhus, K.E.T., Munkejord, S.T., Skaugen, G., 2012. Solution of the span-wagner equation of state using a density-energy state function for fluid-dynamic simulation of carbon dioxide. Ind. Eng. Chem. Res. 51, 1006–1014.
Greenshields, C.J., Weller, H.G., Gasparini, L., Reese, J.M., 2010. Implementation of semi-discrete, non-staggered central schemes in a colocated, polyhedral, finite volume framework, for high-speed viscous flows. Int. J. Numer. Meth. Fl 63, 1–21.
Hafner, A., Forsterling, S., Banasiak, K., 2014. Multi-ejector concept for r744 supermarket refrigeration. Int. J. Refrig. 43, 1–13.
Haida, M., Banasiak, K., Smolka, J., Hafner, A., Eikevik, T., 2016. Experimental analysis of the r744 vapour compression rack equipped with the multi-ejector expansion work recovery module. Int. J. Refrig. 64, 93–107.
Haida, M., Smolka, J., Hafner, A., Palacz, M., Banasiak, K., Nowak, A.J., 2018. Modified homogeneous relaxation model for the r744 trans-critical flow in a two-phase ejector. Int. J. Refrig. 85, 314–333.
Hammer, M., Ervik, A., Munkejord, S.T., 2013. Method using a density-energy state function with a reference equation of state for fluid-dynamic of vapor-liquid–solid carbon dioxide. Ind. Eng. Chem. Res. 52, 9965–9978.
Harten, A., Engquist, B., Osher, S., Chakravarthy, S., 1987. Uniformly high order accuracy essentially non-oscillatory schemes III. J. Comput. Phys. 71, 231–303.
Harvey, A., 2016. Thermophysical properties of carbon dioxide and CO_2-rich mixtures. Technical Report. Applied Chemicals and Materials Division National Institute of Standards and Technology.
Huber, M.L., Sykioti, E.A., Assael, M.J., Perkins, R.A., 2016. Reference correlation of the thermal conductivity of carbon dioxide from the triple point to 1100 k and up to 200 mpa. J. Phys. Chem. Ref. Data 45, 013102.
Jaeger, F., Matar, O.K., Müller, E.A., 2018. Bulk viscosity of molecular fluids. J. Chem. Phys. 148, 174504.
Kunick, M., Kretzschmar, H.J., Gampe, U., 2008. Fast calculation of thermodynamic properties of water and steam in process modelling using spline interpolation. In: Proceedings of the International Conference on the Properties of Water and Steam, Berlin.
Kurganov, A., Noelle, S., Petrova, G., 2001. Semi-discrete central-upwind schemes for hyperbolic conservation laws and Hamilton-Jacobi equations. SIAM J. Sci. Comput 23, 707–740.
Kurganov, A., Tadmor, E., 2001. New high-resolution central schemes for nonlinear conservation laws and convection-diffusion equations. J. Comput. Phys. 160, 241–282.
Lamberts, O., Chatelain, P., Bartosiewicz, Y., 2017. New methods for analyzing transport phenomena in supersonic ejectors. Int. J. Heat. Fluid Flow 64, 23–40.
Lemmon, E.W., Huber, M.L., McLinden, M., 2010. Nist standard reference database 23: reference fluid thermodynamic and transport properties. In: Proceedings of the REFPROP. National Institute of Standards and Technology; Standard Reference Data Program, Gaithersburg.
LeVeque, R.J., 2002. Finite Volume Methods for Hyperbolic Problems. Cambridge University Press, Cambridge, UK.
LeVeque, R.J., Berger, M.J., et al., 2017. Clawpack software. Version 4.3. www.clawpack.org.
Li, D.Q., Groll, E.A., 2004. Transcritical CO_2 refrigeration cycle with ejector-expansion device. Int. J. Refrig. 28, 766–773.
Li, Y.F., Deng, J.Q., Ma, L., Zhang, Y.Z., 2018. Visualization of two-phase flow in primary nozzle of a transcritical CO_2 ejector. Energy Convers. Manag. 171, 729–741.
Liu, J., Chen, J., Chen, Z., 2002. Thermodynamic analysis on trans-critical R744 vapor compression/ejector hybrid refrigeration cycle. In: Proceedings of the 5th IIR-Gustav Lorentzen Conference on Natural Working Fluids, Guangzhou, China.
Lorentzen, G., 1983. Throttling, the internal haemorrhage of the refrigeration process. Proc. Inst. Refrig. 80, 39–47.
Lucas, C., Rusche, H., Schroeder, A., Koehler, J., 2014. Numerical investigation of a two-phase CO_2 ejector. Int. J. Refrig. 43, 154–166.
Masson, N., Jia, H., Burkel, S., 2014. Guide 2014 - Natural refrigerants continued growth & innovation in Europe. Shecco, p. 195.
McAdams, W.H., Woods, W.K., Heroman, L.C., 1942. Vaporization inside horizontal tubes ii-benzene-oil mixture. Trans. ASME 64, 193–200.
Nakagawa, M., Berana, M.S., Harada, A., 2008. Shock waves in supersonic two-phase flow of CO_2 in converging-diverging nozzles. In: Proceedings of the International Refrigeration and Air Conditioning Conference, Purdue, USA.
Nakagawa, M., Berana, M.S., Kishine, A., 2009a. Supersonic two-phase flow of CO_2 through converging-diverging nozzles for the ejector refrigeration cycles. Int. J. Refrig. 32, 1195–1202.
Nakagawa, M., Harada, A., Berana, M.S., 2009b. Analysis of expansion waves appearing in the outlets of two-phase flow nozzles. HVAC&R Res. 15, 1065–1079.
Palacz, M., Haida, M., Smolka, J., Nowak, A.J., Banasiak, K., Hafner, A., 2016. HEM and HRM accuracy comparison for the simulation of CO_2 expansion in two-phase ejectors for supermarket refrigeration systems. Appl. Therm. Eng. 115, 160–169.
Palacz, M., Smolka, J., Fic, A., Bulinski, Z., Nowak, A.J., Banasiak, K., Hafner, A., 2015. Application range of the hem approach for CO_2 expansion inside two-phase ejectors for supermarket refrigeration systems. Int. J. Refrig. 59, 251–258.
Pelanti, M., Shyue, K.M., 2014. A mixture-energy-consistent six-equation two-phase numerical model for fluids with interfaces, cavitation and evaporation waves. J. Comput. Phys. 259, 331–357.
Poinsot, T., Lele, S.K., 1992. Boundary condition for direct simulations of compressible viscous flows. J. Comput. Phys. 101, 104–129.
Raman, S.K., Kim, H.D., 2018. Solutions of supercritical CO_2 flow through a converging-diverging nozzle with real gas effects. Int. J. Heat Mass Transf. 116, 127–135.
Roe, P.L., 1986. Characteristic-based schemes for the euler equations. Ann. Rev. Fluid Mech. 18, 337–365.
Saurel, R., Petitpas, E., Berry, R.A., 2009. Simple and efficient relaxation methods for interfaces separating compressible fluids, cavitating flows and shocks in multiphase mixture. J. Comput. Phys. 228, 1678–1772.
Smolka, J., Bulinski, Z., Fic, A., Nowak, A., Banasiak, K., 2013. A computational model of transcritical R744 ejector based on a homogeneous real fluid approach. Appl. Math. Model. 37, 1208–1224.
Span, R., Wagner, W., 1994. A new equation of state for carbon dioxide covering the fluid region from the triple-point temperature to 1100 K at pressures up to 800 MPa. J. Phys. Chem. Ref. Data 25 (6), 1509–1596.
The National Archives, 2006. Regulation (EC) No 842/2006 of the European Parliament and the Council of 17 May 2006 on certain fluorinated greenhouse gases. OJ L 161, 14.6.2006, p. 1–11 (ES, CS, DA, DE, ET, EL, EN, FR, IT, LV, LT, HU, MT, NL, PL, PT, SK, SL, FI, SV).
Tisza, L., 1941. Supersonic absorption and stokes' viscosity relation. Phys. Rev. 61, 531–536.
Titarev, V.A., Toro, E.F., 2005. Musta schemes for multi-dimensional hyperbolic systems: analysis and improvements. Int. J. Numer. Meth. Fl 49, 117–147.
Toro, E.F., 1997. Riemann Solvers and Numerical Methods for fluids Dynamics. Springer-Verlag, Berlin, Heidelberg.
Toro, E.F., Spruce, M., Speares, W., 1994. Restoration of the contact surface in the HLL Riemann solver. Shock Waves 4, 25–34.
van Leer, B., 1974. Towards the ultimate conservative difference scheme, ii: monotonicity and conservation combined in a second order scheme. J. Comput. Phys. 17, 361–370.
van Leer, B., 1979. Towards the ultimate conservative difference scheme, v: a second-order sequel to Godunov's method. J. Comput. Phys. 54, 101–136.
Vesovic, V., Wakeham, W.A., Olchowy, G.A., Sengers, J.V., Watson, J.T.R., Millat, J., 1989. The transport properties of carbon dioxide. J. Phys. Chem. Ref. Data 19, 763–808.
Yazdani, M., Abbas, A., Radcliff, T., 2014. Numerical modeling and validation of supersonic two-phase flow of CO_2 in converging-diverging nozzles. J. Fluids Eng. 136 (014503).
Yoo, C.S., Im, H.G., 2007. Characteristic boundary conditions for simulations of compressible reacting flows with multidimensional, viscous and reaction effects. Combust. Theor. Model. 11, 259–286.
Zuckerwar, A.J., Ash, R.L., 2006. Variational approach to the volume viscosity of fluids. Phys. Fluids. 8, 047101.